PHYSICAL REVIEW APPLIED **20,** 064012 (2023)

Editors' Suggestion

Superresolution magnetic imaging by a Josephson junction via holographic reconstruction of $I_c(H)$ modulation

Razmik A. Hovhannisyan,[*] Taras Golod, and Vladimir M. Krasnov
Department of Physics, Stockholm University, AlbaNova University Center, Stockholm SE-10691, Sweden

(Received 19 August 2023; accepted 17 November 2023; published 7 December 2023)

This work provides a proof-of-concept for superresolution magnetic imaging using a single Josephson junction. The technique resembles digital holography: magnetic patterns are obtained via an inverse-problem solution from diffractionlike modulation of the junction's critical current, $I_c(H)$. We demonstrate numerical reconstruction of complex two-dimensional patterns, verify the technique experimentally using Nb-based planar junctions, and fabricate an operational sensor on a cantilever. Our results show that Josephson holography allows for both high spatial resolution (approximately 20 nm) and high field sensitivity (approximately 10^{-11} $\mathrm{T}/\sqrt{\mathrm{Hz}}$), thus resolving the trade-off problem between resolution and sensitivity in magnetic scanning probe imaging.

DOI: 10.1103/PhysRevApplied.20.064012

I. INTRODUCTION

Magnetic imaging is a useful microcharacterization tool. Many techniques have been developed over ages for both parallel (such as Bitter decoration [1–3], magneto-optical Kerr-effect microscopy [4,5] and electron holography [6]) and serial (such as Lorentz microscopy [6] and various modifications of scanning probe microscopy (SPM) [7–23]) magnetic imaging. Each of them has some advantages, disadvantages, and limitations depending on field sensitivity, spatial resolution, invasiveness, complexity, sample requirements, etc.

Cryogenic magnetic SPM techniques, such as the scanning superconducting quantum interference device (SQUID) [12–16], Nitrogen-vacancy center (NVC) [18–22] and magnetic force microscopy (MFM) [7–10], achieved remarkable advances in recent decades [23]. However, a common problem of SPM magnetic sensors is a trade-off between spatial resolution and field sensitivity: with decreasing sensor size the resolution is improved but the sensitivity is deteriorated. For example, a SQUID can detect a fraction of flux quantum, Φ_0 [24]. Therefore, its field sensitivity is inversely proportional to the pickup loop area, A. However, the spatial resolution is determined by the loop size. Thus SQUID miniaturization leads to improved resolution at the expense of deteriorated sensitivity. A similar problem exists for NVCs. A single atomic scale NVC could provide a very high spatial resolution, but modest (compared to SQUID) sensitivity [18,19,22]. The sensitivity is limited by the NVC brightness, which could be enhanced by using ensembles of many NVCs at the expense of the reduced spatial resolution [20,21].

Obviation of the trade-off problem requires the development of superresolution microscopy. This concept is well known from optics, where it refers to the resolution better than the diffraction limit [25–28]. In magnetic SPM, it implies the spatial resolution better than the sensor size. In Refs. [29–31] it was suggested that a single planar Josephson junction (JJ) can be used for superresolution magnetic imaging. The main idea is that a local inhomogeneous magnetic field, H^*, is encoded in the modulation of the Josephson critical current versus external homogeneous magnetic field, $I_c(H)$ and could be reconstructed via the inverse-problem solution from the diffractionlike $I_c(H)$ pattern in a manner similar to digital holography in optics [32,33]. In Ref. [31] this was demonstrated for a special case of symmetric $H^*(x)$. However, application of this idea for SPM imaging requires a general inverse-problem solution for arbitrary (asymmetric) field distribution.

This work represents both theoretical and experimental development of practical Josephson holography. Theoretically, a general inverse-problem solution is obtained and superresolution imaging of complex magnetic objects is demonstrated. The technique is verified experimentally using Nb-based planar JJs. We demonstrate successful reconstruction of fields from an MFM tip and an Abrikosov vortex, and an operational SPM sensor fabricated on a cantilever. Finally, we discuss the procedure of holographic

---

[*] razmik.hovhannisyan@fysik.su.se

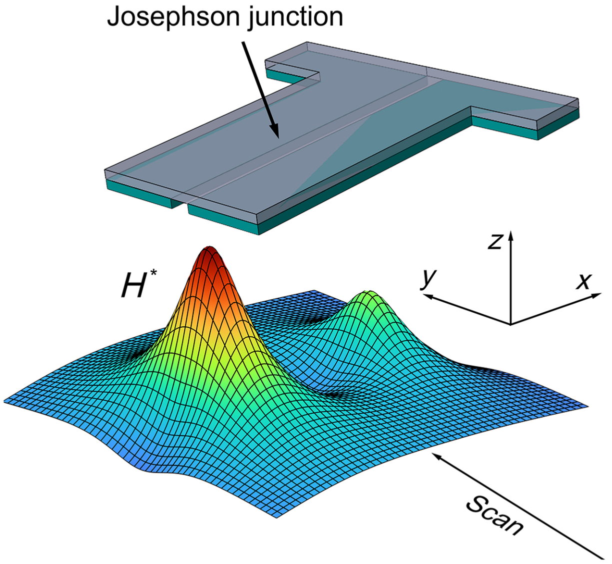

FIG. 1. A sketch of the proposed Josephson holography. A planar Josephson junction is employed as a scanning probe sensor for imaging of an inhomogeneous field $H^*(x,y)$. The 2D map is obtained in a single linear scan along the y axis. At every y point of the scan the $I_c(H)$ modulation is measured and the complete $H^*(x, y = \text{const})$ profile is reconstructed via the inverse-problem solution.

SPM imaging, its resolution, optimal sensor geometry and figure of merit. We conclude that the superresolution ability of Josephson holography enables both high resolution (approximately 20 nm) and high sensitivity ($\sim 10^{-11}$ T/$\sqrt{\text{Hz}}$), thus resolving the trade-off problem.

II. RESULTS

A. Josephson holography

Figure 1 represents a sketch of the considered geometry: a magnetic object, creating a two-dimensional (2D) inhomogeneous field, $H^*(x,y)$, is being probed by a planar JJ with the length L along the x axis. Josephson effect appears as a result of quantum mechanical interference of electronic wave functions from two superconducting electrodes, leading to Fraunhofer-type $I_c(H)$ modulation. The inhomogeneous field, $H^*(x)$, distorts the $I_c(H)$ modulation due to appearance of an additional phase shift, $\varphi^*(x)$, within the JJ [30]. We aim to reconstruct object-induced $\varphi^*(x)$ and $H^*(x)$ from the analysis of diffractionlike $I_c(H)$ modulation. The method resembles digital holography [32,33] with $I_c(H)$ patterns serving as holograms [31].

The key obstacle for solving the corresponding inverse problem is in the unknown phase offset, ϕ, which should be obtained from an additional condition for maximization of the Josephson current (see Appendix A). Symmetric with respect to the junction center case is the only lucky exception, for which $\phi = \pm\pi/2$ is well defined, thus enabling a simple analytic solution [31]. However, any type of asymmetry, either external, $H^*(x)$, or internal in the JJ, disables this possibility. Figure 2 illustrates the behavior of a junction with an asymmetric internal distribution of the critical current density, $J_c(x)$, shown by the red line in Fig. 2(a). Red lines represent calculated characteristics (direct problem solutions) (a)–(c) in the absence of the magnetic object, $H^* = 0$, and (d)–(f) with an asymmetric $H^*(x)$ shown by the red line in Fig. 2(d). Magnetic fields are normalized by the flux quantization field, H_0, of the JJ. Complicated $\phi(H)$ dependencies, shown by red lines in Figs. 2(b) and 2(e), appear in both cases. Therefore, a straightforward inverse solution is precluded for asymmetric cases.

The uncertainty of ϕ resembles the phase problem in optical holography [35–37]. Inspired by optical phase retrieval algorithms [35], we developed a numerical procedure for obtaining a general inverse solution for arbitrary $J_c(x)$ and $H^*(x)$ (see Appendices B–D). Black-dashed lines in Figs. 2(e) and 2(d) show thus reconstructed $\phi(H)$ and $H^*(x)$ dependencies, obtained from $I_c(H)$ modulation from Fig. 2(f), truncated at $H_{\max} = 50H_0$. The perfect coincide with actual dependencies shown by red lines confirms the accuracy of the inverse-problem solution in the asymmetric case. The spatial resolution is apparently not limited by the junction length, L, confirming the superresolution.

B. SPM imaging procedure

In all SPM techniques, to date, the 2D map is acquired via raster scanning of the object. The proposed holographic imaging by a JJ is quite different because it provides a complete one-dimensional (1D) field distribution within the junction at every position of the sensor. Therefore, the 2D image can be obtained from a single linear (1D) scan, as sketched in Fig. 1. However, at every point of the scan, a detailed measurement of $I_c(H)$ should be performed.

To clarify the imaging procedure we consider the case shown in Fig. 1. The linear scan is made along the y axis. Figure 3(a) shows the color map of the test $H^*(x,y)$ containing two dissimilar peaks with the widths at half-maximum, $\sigma \simeq 0.2\,L$. Figure 3(b) represents the hologram, i.e., the $I_c(H,y)$ plot calculated at every point of the scan, using the corresponding $H^*(x, y = \text{const})$ cross sections. Three of them at $y = 0$, $0.2L$, and $0.4L$ are shown by red lines in Fig. 3(c). Black and green dashed lines in Fig. 3(c) represent reconstructed field profiles obtained from $I_c(H,y)$ with truncated integration ranges at $H_{\max} = \pm 50$ and ± 10 H_0, respectively. Both reconstructions provide accurate shapes of the peaks, but narrower $I_c(H)$ truncation leads to parasitic oscillations at the periphery. Figures 3(d) and 3(e) represent reconstructed 2D maps $H^*(x,y)$ obtained for $H_{\max}/H_0 = 50$ and 10. A comparison with Fig. 3(a) shows that the reconstruction with $H_{\max}/H = 50$ is almost perfect. For $H_{\max}/H = 10$, it is

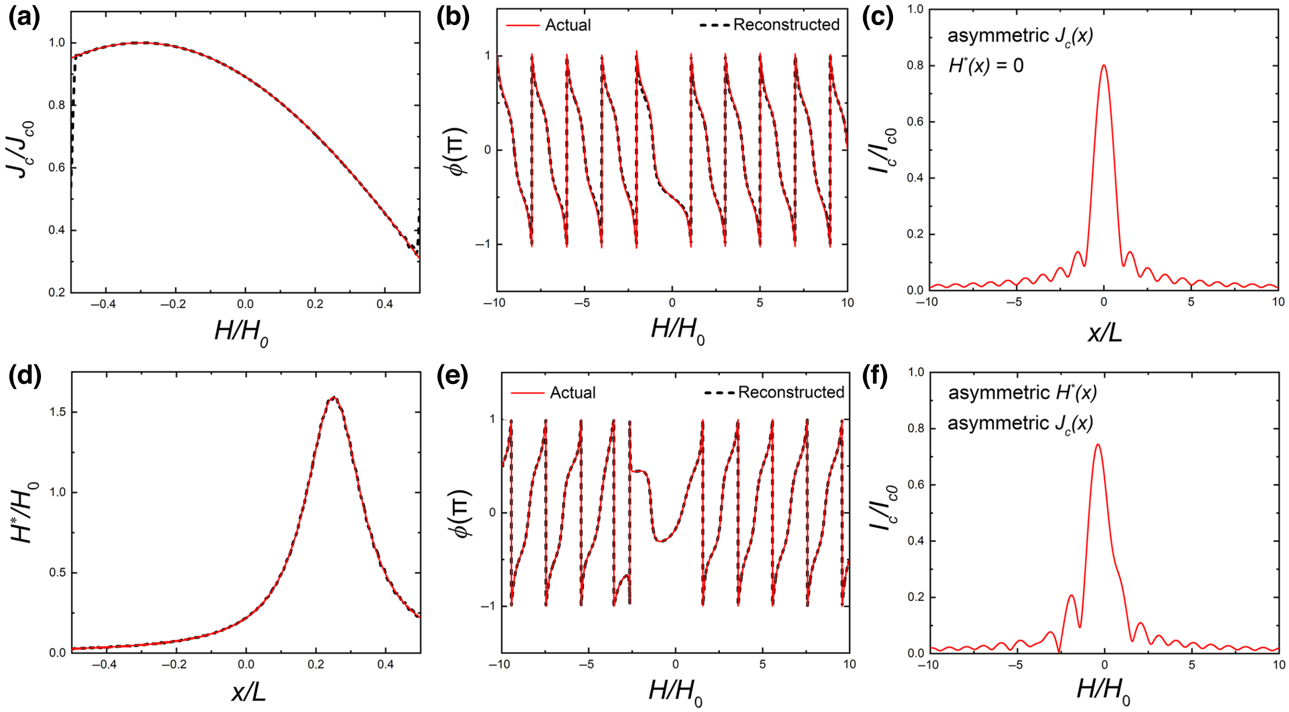

FIG. 2. Direct (red) and inverse (black-dashed lines) problem solutions for an asymmetric case. (a)–(c) Without inhomogeneous field and (d)–(f) with an asymmetric $H^*(x)$, shown in (d). (a) Critical current density distribution within the junction. (b) $\phi(H)$ and (c) $I_c(H)$ dependencies for $H^* = 0$. Black dashed lines in (b) and (c) illustrate the junction calibration procedure according to Ref. [34]. (d) and (e) show calculated $\phi(H)$ and $I_c(H)$ for the asymmetric $J_c(x)$ from (a) and the asymmetric single-peak $H^*(x)$ from (d). Inverse solutions (black) are obtained with integral truncation at $H_{\max} = 50H_0$.

very good, but some truncation-related oscillations are visible. Various types of image improvements can be used as discussed in Ref. [31] and Appendix E.

In Fig. 4 we show the reconstruction of a more complex pattern, containing very small and sharp features.

C. Experimental verification

Abrikosov vortex is an example of a nanoscale magnetic object. Stray fields of a vortex trapped in the junction electrode create a well-defined local field in the JJ, which depends solely on the geometry [38–41]. The well-calibrated nature of this field ideally suits for the verification [31]. Figure 5(a) shows a SEM image of a sample, similar to that studied in Ref. [31], containing an Nb-based planar JJ with $L = 5.4$ μm and an artificial vortex trap at a distance $z_V = 360$ nm. Figure 5(b) shows measured $I_c(H)$ modulation patterns without trapped vortex (blue) and with a trapped antivortex (red) at $T = 6.6$ K. The black line in Fig. 5(c) represents the reconstructed $H^*(x)$ alongside the anticipated stray field of the antivortex for the given sample geometry (red curve). The agreement is very good without any fitting. The width at half maximum is $\sigma \simeq 500$ nm $< 0.1\ L$ confirming the superresolution. However, the accuracy is much better than that. The inset in Fig. 5(c) shows a closeup on the half-maximum region, from which it is seen that the actual spatial accuracy of reconstruction is $\Delta\sigma \simeq 20$ nm.

Figure 6 represents an example of reconstruction of the field from an external magnetic object—an MFM tip placed above the planar JJ, as sketched in the inset. The sensor JJ is similar to that in Fig. 5(a). The experiment was performed in a low-temperature MFM setup, for details see Refs. [10,40] and their Supplemental Material. The MFM tip creates a monopolelike field with a maximum value $\simeq 190$ Oe [42], which is too large for a JJ. To reduce it, we lifted the tip at a significant height $h \simeq 1.7$ μm above the center of the JJ. Black symbols in Fig. 6(a) show thus measured $I_c(H)$ modulation of the JJ. It is strongly distorted indicating that the tip is quite invasive even at such height. The black line in Fig. 6(b) shows reconstructed tip-induced phase shift $\varphi^*(x)$. The blue line represents a smooth fit, the derivative of which yields the tip-induced field. It is shown by the blue line in Fig. 6(c). The red line in (c) represents the expected monopolelike field at the given tip-JJ height of $\simeq 1.7$ μm (see Appendix F for more details). The agreement is good. To cross-check the correctness, we also calculated the expected $I_c(H)$ modulation for the reconstructed φ^*. It is shown by the red line in Fig. 6(g). It is consistent with the experimental $I_c(H)$, confirming the validity of the reconstruction.

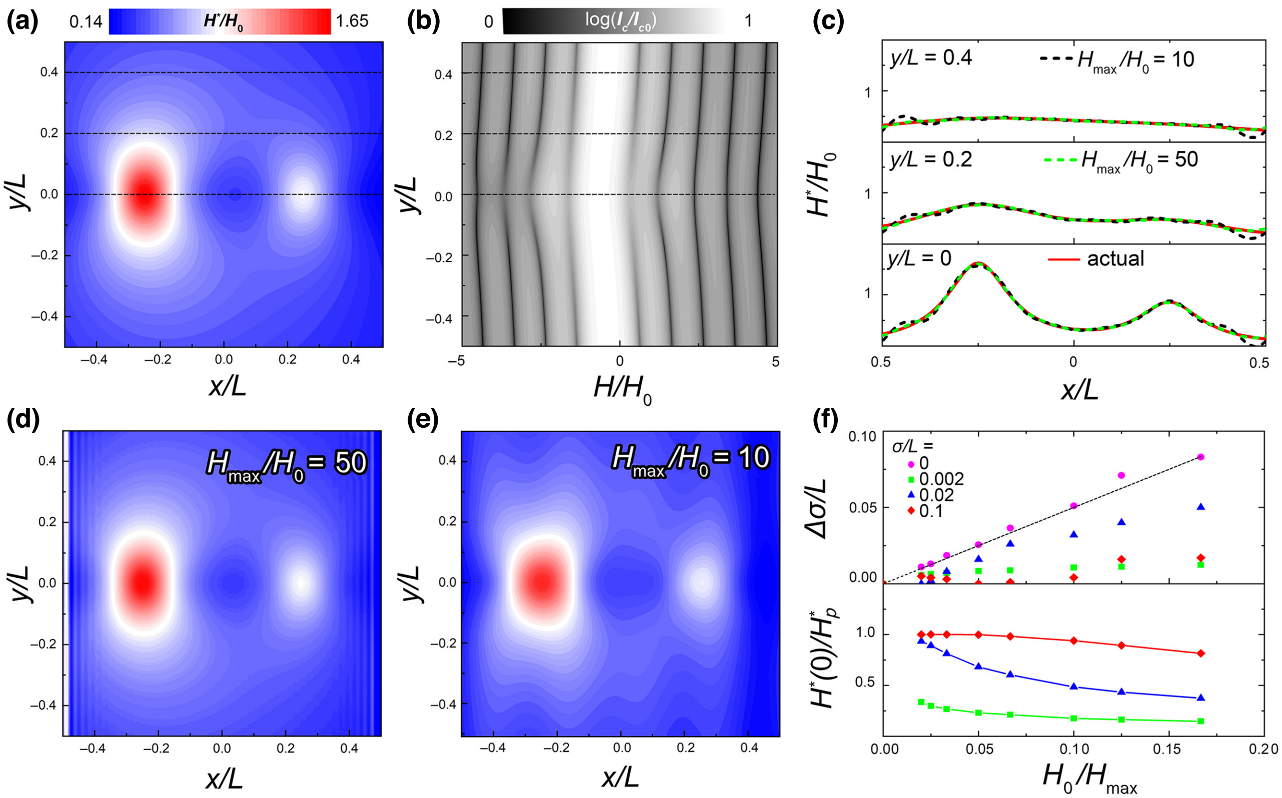

FIG. 3. Holographic reconstruction of an asymmetric double-peak structure depicted in Fig. 1. (a) Color map of the actual $H^*(x, y)$. (b) Calculated $I_c(H, y)$ hologram. (c) Red lines show $H^*(x, y = \text{const})$ cross sections at three y positions, indicated by dashed lines in (a) and (b). Black and green lines show reconstructed profiles for $H_{\max}/H_0 = 10$ and 50, respectively. (d),(e) show reconstructed 2D maps for $H_{\max}/H_0 = 50$ and 10. (f) The accuracy of reconstruction of the width (top) and the height (bottom) as a function of the reciprocal field range, $H_0/H_{\max}$, for a single peak with different widths at half-maximum: $\sigma/L = 0$ (magenta circles), 0.002 (green squares), 0.02 (blue triangles), and 0.1 (red rhombuses).

To demonstrate the feasibility of holographic SPM imaging, we fabricated several sensors on cantilevers of commercial atomic force microscope (AFM) tips, see Appendix G. Figures 7(a) and 7(b) show SEM images of one of the sensors. It contains a planar Nb JJ with the length $L \simeq 5.3$ μm and a Pt tip enabling topographic AFM scanning. Figure 7(c) shows measured $I_c(H)$ modulation of this sensor at $T \simeq 3.2$ K. A clear Fraunhofer-type modulation indicates good quality of the JJ. Various design improvements were discussed in Ref. [29]. The most interesting is the implementation of an additional electrode, which would enable control-line operation through one

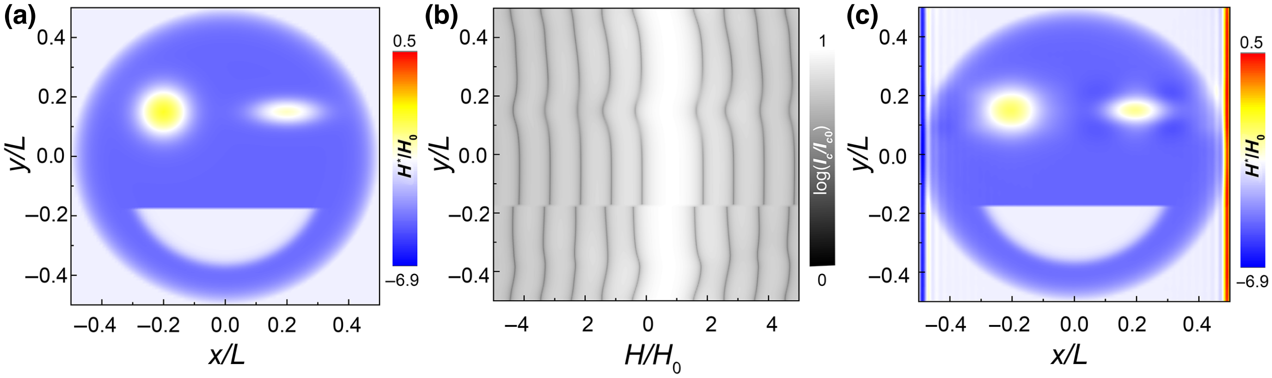

FIG. 4. Demonstration of a more complex 2D reconstruction. (a) The original $H^*(x, y)$ map (the smiles). (b) The corresponding $I_c(H, y)$ hologram. (c) Reconstructed pattern using the hologram from (b) with $H_{\max}/H_0 = 50$.

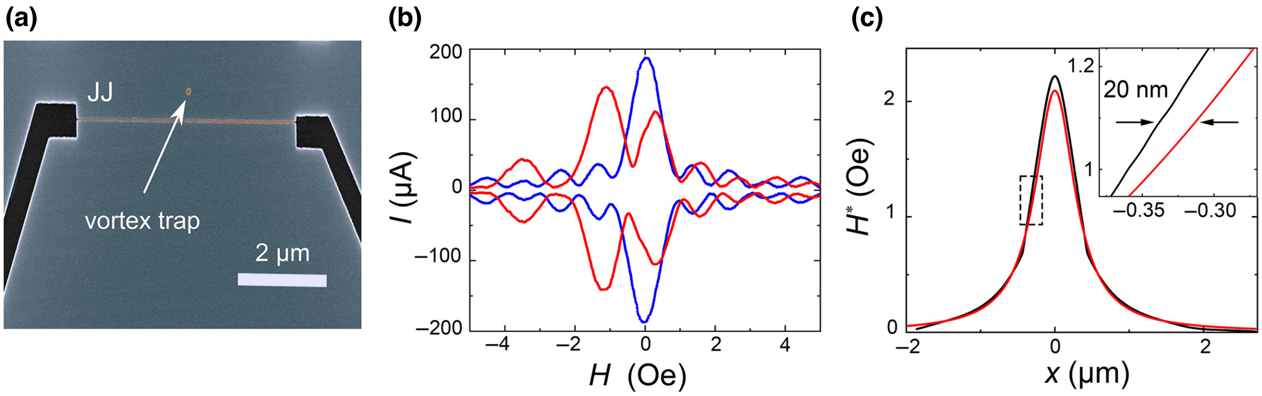

FIG. 5. Experimental reconstruction of stray fields from an Abrikosov vortex. (a) SEM image of a planar junction with a vortex trap. (b) Measured $I_c(H)$ patterns without a vortex (blue) and with a trapped antivortex (red). (c) Black line represents the field profile reconstructed from the experimental $I_c(H)$ in (b). Red line shows the anticipated stray field for the actual sample geometry. The inset shows a closeup in the half-maximum range, which indicates the spatial accuracy of reconstruction approximately 20 nm.

of the junction electrodes [29]. This would allow broad-range measurements of junction's $I_c(H)$ with minimal invasiveness on the imaged object.

III. DISCUSSION

A. Resolution

Resolution of optical holography deteriorates with decreasing of the number of stored interference fringes, which occurs upon truncation of the hologram (reduction of an aperture) and/or reduction of the object size [32]. Similarly, spatial resolution of our method is limited only by the number of lobes in the $I_c(H)$ pattern, i.e., by the field range $H_{\max}/H_0$ [31], and depends on the shape and size of the object.

Figure 3(f) summarizes the accuracy of reconstruction of an isolated peak [see Fig. 2(d)] with different widths, $\sigma/L = 0$ (magenta), 0.002 (green), 0.02 (blue), and 0.1 (red symbols), as a function of the reciprocal field range $H_0/H_{\max}$. The top panel shows the error of width reconstruction, $\Delta\sigma/L$. The bottom panel shows the reconstructed peak height $H^*(0)$ normalized by the actual height, H_p^*. Generally, for a given range $H_{\max}/H_0$ the accuracy becomes better [$\Delta\sigma \to 0$ and $H^*(0)/H_p^* \to 1$] with increasing the object size, σ. The most difficult is to resolve a δ-function peak [$\varphi^* = \theta(x)$—the Heaviside function], for which truncation-related oscillations are difficult to dampen. The black line represents half the wavelength of such oscillations, $\lambda/2 = (H_0/2H_{\max})L$, which apparently defines the spatial resolution for $\sigma = 0$. For $\sigma/L = 0.002$ (green) the width accuracy seems to be very good, but the peak height is strongly underestimated. Thus, the overall (spatial and field) resolution does depend on the object's shape and size. The linear growth, seen in the top panel of

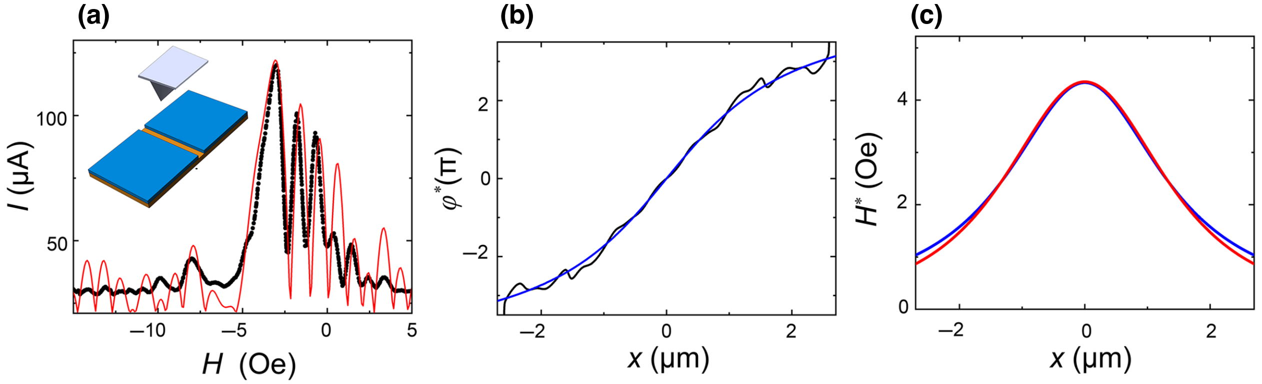

FIG. 6. Demonstration of holographic reconstruction of magnetic field from an MFM tip. (a) Black symbols shows measured $I_c(H)$ pattern with a deployed tip. The red line shows $I_c(H)$ calculated using the reconstructed $H^*(x)$ from (c). (b) Black line represents the reconstructed tip-induced phase shift. The blue line is the smoothing spline. (c) The blue line represents the reconstructed field of the tip. The red line shows the anticipated monopolelike tip field calculated for the actual tip-junction distance of 1.7 μm.

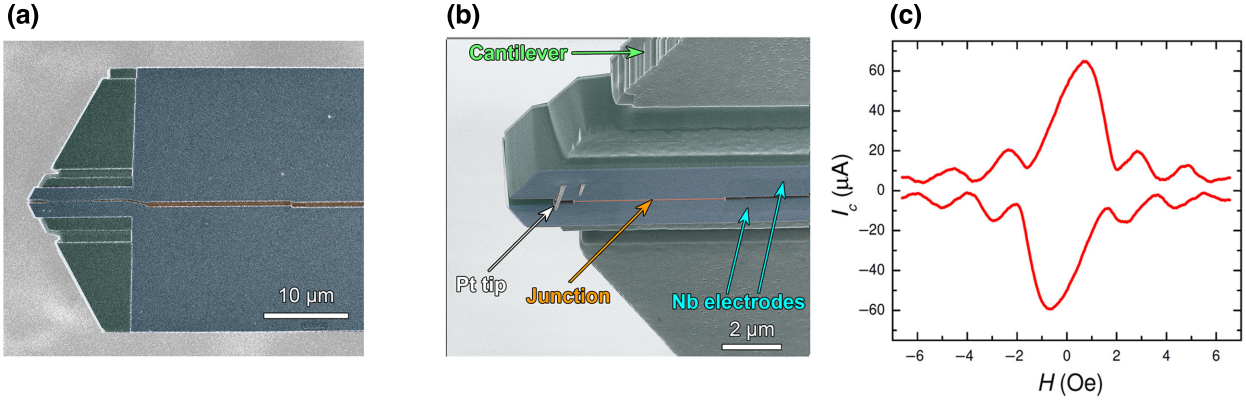

FIG. 7. Demonstration of an operational holographic sensor for scanning probe microscopy. (a),(b) SEM images (false color) of a sensor fabricated on a cantilever of an AFM tip. It contains two Nb electrodes [broad horizontal bands, separated by a FIB cut, painted orange in (a)] and a variable-thickness-bridge-type Josephson junction [a thin horizontal line at the left end of the cantilever, painted orange in (b)], made by focused ion-beam etching. In addition, a Pt tip was grown by EBID to enable AFM operation. (c) Measured $I_c(H)$ modulation of the sensor junction at $T = 3.24$ K.

Fig. 3(f) indicates that the spatial accuracy can be written as

$$\Delta\sigma = \alpha \frac{H_0}{H_{\max}} \frac{L}{2}, \tag{1}$$

where $\alpha < 1$ depends on the size of the imaged object. For experimentally easily accessible field range $H_{\max} = 10H_0$, objects with size $\sigma = 0.1\,L$ can be resolved with the accuracy of field determination of 96% and a remarkable (nm-range) spatial accuracy $\delta\sigma \simeq 0.004\,L$, fully consistent with our estimation in the inset of Fig. 5(c).

B. Optimal sensor geometry

From Fig. 3(f) it follows that accurate spatial and field reconstruction requires fairly broad $I_c(H)$ holograms with the field range $H_{\max} \sim 10H_0$. This field should be fairly small, $H_{\max} \lesssim 10$ Oe, to remain noninvasive for the imaged object and to avoid entrance of Abrikosov vortices in junction electrodes. As seen from Fig. 5(b) vortices strongly distort the $I_c(H)$ pattern [39] and, therefore, hamper the reconstruction. For planar JJs [43]

$$H_0 = 1.8 \frac{\Phi_0}{L^2}. \tag{2}$$

Obtaining ten lobes at $H_{\max} < 10$ Oe requires that the junction length should not be less than $L = 6$ μm. In the considered case, $H_{\max}/H_0 = 10$ and $L = 6$ μm, Eq. (1) yields $\Delta\sigma = \alpha L/20 = \alpha \cdot 300$ nm. As can be seen from Fig. 3(f), for objects with size $\sigma = 0.1\,L = 600$ nm, $\alpha \simeq 0.07$, and $\Delta\sigma \simeq 20$ nm. This implies that for a ferromagnetic domain with the width of 600 nm, domain edges will be imaged with the 20-nm resolution. This can be seen, from the reconstruction from Fig. 4, where the sharp edges of the mouth of the smilis are perfectly resolved. Experimental data from Fig. 5(c) confirms that for a planar JJ with the size $L = 5.4$ μm the spatial accuracy of 20 nm can be achieved in a small field range $H_{\max} \sim 6$ Oe.

From Eqs. (1) and (2) it follows,

$$\Delta\sigma = 0.9\alpha \frac{\Phi_0}{H_{\max} L}. \tag{3}$$

Thus, the spatial resolution depends on the size of the junction and the maximal field range. There is some flexibility in the choice of parameters: it is possible to tune the spatial resolution by varying L and $H_{\max}$. Interestingly, Eq. (3) leads to a counterintuitive conclusion that for a fixed field range $H_{\max}$, larger junctions have a better spatial resolution. However, there is a limit for increasing the junction size: the JJ should remain in the "short" limit, which means that L should not exceed 4 times the Josephson penetration depth, $L < 4\lambda_J$. For planar JJs, $\lambda_J \propto 1/\lambda^2 I_c(0)$ [43,44], where λ is the London penetration depth. Although λ_J could be tuned by fabrication and operation temperature, yet we believe that it would be unpractical to increase the junction size above approximately 6 μm because larger junctions would be prone to trapping Abrikosov vortices.

C. Sensor figure of merit

As discussed in the Introduction, magnetic SPM sensors suffer from the trade-off problem between spatial resolution, δx, and field sensitivity, δH. For example, SQUIDs are flux detectors with a typical flux noise $S_\Phi \sim 10^{-7} - 10^{-6}\ \Phi_0/\sqrt{\mathrm{Hz}}$ [12,13,24]. The field sensitivity, $\delta H = \delta\Phi/A$, is inversely proportional to the pickup loop area, A. However, the spatial resolution is determined by the loop size, $\delta x \sim \sqrt{A}$. Thus SQUID miniaturization leads to improved resolution at the expense of deteriorated sensitivity. The product, $\delta H \delta x^2 \simeq S_\Phi$, remains approximately independent of the pickup loop size. Therefore, we can introduce a universal figure of merit for magnetic SPM sensors:

$$\mathrm{FM} = \frac{\Phi_0}{\delta x^2 \delta H}. \tag{4}$$

For SQUIDs, $\mathrm{FM} \simeq \Phi_0/S_\Phi \sim 10^6 - 10^7\ \sqrt{\mathrm{Hz}}$. Interestingly, similar FM values can be obtained for top-performance cryogenic NVC and MFM sensors [23]. For example, a single NVC sensor could provide a very high spatial resolution, $\delta x \sim 20$ nm, with field sensitivity $3 \times 10^{-7}\ \mathrm{T}/\sqrt{\mathrm{Hz}}$ at 4.2 K [22], leading to $\mathrm{FM} \sim 10^7\sqrt{\mathrm{Hz}}$.

For a superresolution sensor based on a planar JJ, the field sensitivity is determined by H_0, Eq. (2), which yields the effective junction area $A = L^2/1.8$ [29]. However, the spatial resolution is not limited by L. Therefore, the figure of merit acquires an additional factor,

$$\mathrm{FM}_{\mathrm{JJ}} \sim \frac{L^2}{\delta x^2}\mathrm{FM}_{\mathrm{SQUID}}. \tag{5}$$

Here the factor $(L/\delta x)^2 > 1$ reflects the improvement due to superresolution. Hypothetically, it could be arbitrary large, limited only by the size of the hologram, $H_{\max}/H_0$. In reality, however, $H_{\max}$ is limited because large fields are invasive both for the object and the junction. The experimental analysis in Fig. 5(c) indicates that a spatial accuracy of 20 nm can be achieved using a planar JJ with the size $L = 5.4\ \mu$m, flux quantization field $H_0 \simeq 1$ Oe and with an estimated field sensitivity $\delta H \simeq 10^{-11}\ \mathrm{T}/\sqrt{\mathrm{Hz}}$. This suggests more than 4 orders of magnitude enhancement of the figure of merit, $\mathrm{FM}_{\mathrm{JJ}} \sim 5 \times 10^{11}\sqrt{\mathrm{Hz}}$, as a consequence of superresolution.

IV. CONCLUSION

To conclude, we proved the feasibility of superresolution magnetic imaging via Josephson holography. We developed a simple phase-retrieval algorithm, which enables a general inverse-problem solution. Various examples of superresolution imaging of complex magnetic patterns were demonstrated. Experimentally, we verified the technique using Nb-based planar JJs and demonstrated an operational SPM sensor on a cantilever. We showed that Josephson holography allows practically achievable spatial accuracy approximately 20 nm while retaining very high field sensitivity approximately $10^{-11}\ \mathrm{T}/\sqrt{\mathrm{Hz}}$, thus resolving the trade-off problem in magnetic scanning probe imaging.

ACKNOWLEDGEMENTS

We are grateful to A.L. Shilov for stimulating discussions and to V.V. Dremov, S.Yu. Grebenchuk, and V.S. Stolyarov for assistance with the MFM experiment, which was performed at the Moscow Institute of Physics and Technology.

APPENDIX A: JOSEPHSON HOLOGRAPHY PRINCIPLES

We assume that the sensor JJ is in the short limit, which allows us to neglect screening effects and to assume that the magnetic induction inside the junction is a superposition of the inhomogeneous $H^*(x)$ from the object and the homogeneous external field H,

$$B(x) = H + H^*(x). \tag{A1}$$

It causes a Josephson phase gradient in the JJ,

$$\frac{\partial \varphi}{\partial x} = \alpha B(x), \tag{A2}$$

where $\alpha = 2\pi/LH_0$. From Eqs. (A1) and (A2), the phase distribution inside the JJ can be written as [30]

$$\varphi(x) = \alpha H x + \varphi^*(x) + \phi, \tag{A3}$$

where

$$\varphi^*(x) = \alpha \int_{-L/2}^{x} H^*(\xi) d\xi, \tag{A4}$$

is the phase shift induced by the object and ϕ is a phase offset. The local supercurrent density within the junction is given by the Josephson current-phase relation,

$$J(x) = J_c(x) \sin \varphi(x), \tag{A5}$$

where $J_c(x)$ is the local critical-current density. The critical current can be written as a Fourier integral [31]

$$iI_c(H) = \int_{-L/2}^{L/2} J_c(x) \exp i\left[\alpha H x + \varphi^*(x) + \phi\right] dx, \tag{A6}$$

in which the offset ϕ maximizes I_c,

$$\frac{\partial I_c}{\partial \phi} = 0. \tag{A7}$$

In the homogeneous case, $H^* = 0$, $J_c = \mathrm{const}$, Eq. (A6) leads to the Fraunhofer $I_c(H)$ modulation, characteristic for light diffraction from a single slit with uniform illumination. In the inhomogeneous case, the $I_c(H)$ modulation is distorted [30]. As follows from Eq. (A6), this is equivalent to diffraction with both nonuniform illumination [$J_c(x)$ prefactor] and an additional phase shift within the slit [$\varphi^*(x)$ under the exponent]. Of those only $\varphi^*(x)$ carries information about the object, while $J_c(x)$ is an intrinsic property of the junction (light source imperfection in optics). Our task is to reconstruct the unknown $\varphi^*(x)$ from the known $I_c(H)$ modulation. This requires an inverse solution of Eq. (A6) together with Eq. (A7). In Ref. [31], a solution was found for a special case of symmetric $H^*(x)$. Our goal is to find a general solution for arbitrary H^*.

As shown in Ref. [31], the inverse Fourier transform of Eq. (A6), followed by the division of its imaginary and real parts, leads to the expression for $\varphi^*(x)$, independent of junction imperfection, $J_c(x)$:

$$\tan\varphi^*(x) = \frac{\int_{-\infty}^{\infty} I_c(H)\cos[\alpha x H + \phi(H)]dH}{\int_{-\infty}^{\infty} I_c(H)\sin[\alpha x H + \phi(H)]dH}. \tag{A8}$$

It contains the unknown offset, ϕ, which should be obtained from Eq. (A7). As shown in Ref. [31], this yields

$$\tan\phi(H) = \frac{\int_{-L/2}^{L/2} J_c(x)\cos\left[\alpha H x + \varphi^*(x)\right]dx}{\int_{-L/2}^{L/2} J_c(x)\sin\left[\alpha H x + \varphi^*(x)\right]dx}. \tag{A9}$$

Generally, ϕ is a complicated function of H, $J_c(x)$, and $\varphi^*(x)$, as can be seen from Figs. 2(b) and 2(e). The implicit interrelation of φ^* and ϕ in integral Eqs. (A8) and (A9) precludes a straightforward analytic solution.

APPENDIX B: PHASE-RETRIEVAL ALGORITHM

The unknown offset ϕ is the key obstacle for solving Eq. (A8). This resembles the phase problem in optics, for which several phase-retrieval algorithms were developed [35–37]. Inspired by the Gerchberg-Saxton algorithm [35], we develop the following iterative procedure for solving coupled integral Eqs. (A8) and (A9).

Step 1, junction calibration. JJs may contain imperfections, $J_c(x) \neq \text{const}$. Since $J_c(x)$ enters in Eq. (A9), it cannot be ignored. Therefore, at the first step, the junction should be calibrated without a magnetic object, to obtain $J_c(x)$. In SPM this can be easily done by lifting the sensor well above the sample. Figure 2(a) shows an example of calculated $I_c(H, \varphi^* = 0)$ modulation for the asymmetric $J_c(x)$, shown by the red line in Fig. 2(a). It can be seen that the inhomogeneity of $J_c(x)$ distorts the $I_c(H)$ with respect to the ideal Fraunhofer modulation. The red line in Fig. 2(b) shows a nontrivial $\phi(H)$ dependence in this case. The procedure for extracting $J_c(x)$ from $I_c(H, \varphi^* = 0)$ is well known [34]. Black dashed lines in Figs. 2(b) and 2(a) represent the $\phi(H)$ and $J_c(x)$ reconstructed from the $I_c(H, \varphi^* = 0)$. A perfect agreement between the actual (red) and reconstructed (black) $J_c(x)$ indicates the successful calibration.

Step 2, iterations. Equations (A8), (A9) are solved iteratively, starting from some initial guess $\varphi_0^*(x)$. The nth iteration step starts with substitution of the previous φ_{n-1}^* value in Eq. (A9) to obtain ϕ_n, which is subsequently substituted in Eq. (A8) to obtain another φ_n^*. The procedure is rapidly converging, as discussed in the section Appendix D. Finally, $H^*(x)$ is obtained from

$$H^*(x) = \frac{1}{\alpha}\frac{\partial\varphi^*(x)}{\partial x}. \tag{B1}$$

APPENDIX C: RECONSTRUCTION OF $J_c(x)$: LOGARITHMIC HILBERT TRANSFORMATION

The reconstruction technique of $J_c(x)$ proposed in Ref. [34] requires a logarithmic Hilbert transformation to determine the term $\phi(H)$ [see Eq. (A6)], which is the key obstacle for achieving a correct inverse Fourier transform [31]. This approach is based on the calculation of the convolution ($\circledast$) of two functions: $\ln I_c(\beta)/\beta$ and $1/\beta$, where $\beta = \alpha HL$. However, the integrand function has an infinite number of singularity points at the magnetic fields where $I_c(H) = 0$. For these reasons, in our work, we have used one of the most convenient and accurate methods for calculating the logarithmic Hilbert transformation Ref. [45]:

$$\phi = \frac{\beta}{\pi}\mathscr{F}^{-1}(\{[-i\pi\ \mathrm{sgn}(x)] \circledast \mathscr{F}[\mathrm{I_c}(\beta)]\}[-i\pi\ \mathrm{sgn}(x)]),$$

where $\mathscr{F}$ and $\mathscr{F}^{-1}$ represent the direct and inverse Fourier transforms, respectively, and $\mathrm{sgn}(x)$ denotes the signum function.

APPENDIX D: CONVERGENCE OF ITERATION SCHEMA

Figure 8 demonstrates the reconstructed phase $\varphi^*(x)$ at different iterations. As can be seen in the first step, the initial guess was taken as a linear function with a tilt equal to the shift of the main peak of the $I_c(H)$ dependency.

Furthermore, it is evident that less than 20 steps are sufficient for the curve to converge completely to the actual one.

APPENDIX E: METHOD OF IMAGE IMPROVEMENT: FOURIER FILTERING

Figure 9 depicts the $H^*(x)$ dependency for the case presented in Fig. 4 at $y/L = -0.3$. The red line represents the actual H^*, while the blue curve represents the H^* directly reconstructed for $H_{\max}/H_0 = 50$. Noticeably, parasitic short-wavelength oscillations are visible in the blue curve. However, since they are well separated from the low wave-number part, which represents the actual $H^*(x)$ variation, they can be easily removed using proper band-pass filtering. The result of such filtering is depicted in Fig. 9 by the black dashed line.

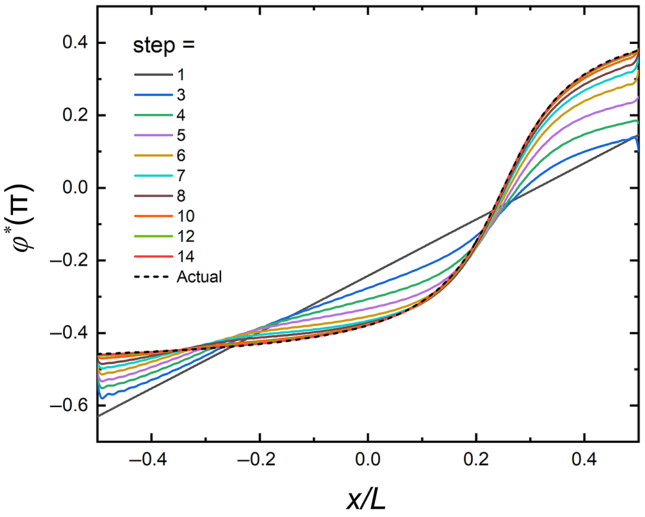

FIG. 8. Calculated by Eqs. (A8) and (A9) dependency $\varphi_n^*(x)$ on different steps of iterations. The reconstruction has been carried out for $J_c(x)$ and $I_c(H)$ dependency shown on the Figs. 2(c) and 2(d), respectively.

APPENDIX F: MFM MEASUREMENTS

Measurements of the critical current in the field of MFM tip were conducted using the low-temperature SPM system (AttoCube AttoDry 1000) at a temperature $\simeq 6.5$ K. We use a commercial Co/Cr-coated MFM tip Bruker, MESP V2. For performing the MFM experiment, shown in Figs. 6(a)–6(c), the topography of the sample was first imaged in the atomic-force-microscopy mode. After that, the tip was placed above the center of the junction and retracted to the height of approximately 1.7 μm. Subsequently, $I_c(H)$ measurements were done with a stationary tip, Fig. 6(a).

As shown in Ref. [42], the field of this MFM tip is well described by a magnetic monopole with the magnetic charge Q_M, placed at some height h_0 above the tip end:

$$H^*_{\text{tip}} = \frac{Q_M}{4\pi\mu_0}\frac{\mathbf{r}}{r^3}.$$

The tip-induced local field at the JJ depends on Q_M, h_0, and the height of the tip with respect to the junction plain, h. Tip parameters vary slightly, depending on experimental conditions, in the range of $Q_M = 2 - 8 \times 10^{-14}$ Wb and $h_0 = 200 - 400$ nm for the used tip type [42]. The estimation of the tip field, shown in Fig. 6(c), corresponds to $Q_M = 2.0 \times 10^{-14}$ Wb, $h_0 = 300$ nm and $h = 1.65$ μm. It represents the out-of-plain component, $H^*(x)$, of the monopole field.

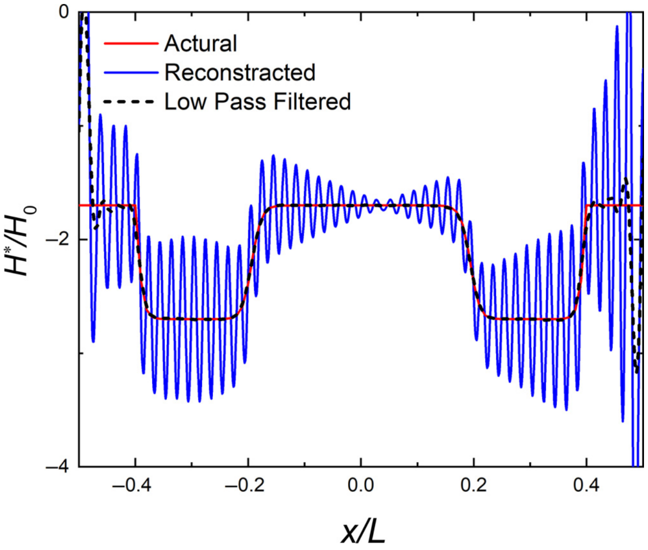

FIG. 9. Reconstructed field for Fig. 4 at $y/L = -0.3$. The red line shows the actual $H^*(x)$. The blue line shows a nonfiltered reconstructed image from $I_c(\Phi)$ truncated at $H_{\max}/H_0 = 50$. Short wavelength oscillations, caused by the truncation, are clearly seen. The black line shows the same curve processed by low-pass Fourier filtering of parasitic oscillations.

APPENDIX G: SAMPLE FABRICATION

The sensor was made in the following way: First, a 70-nm-thick Nb film was deposited on one side of the cantilever using magnetron sputtering. Subsequently, the electrodes were made by Ga focused ion-beam (FIB) etching. The junction was made by cutting a narrow groove (approximately 30 nm) in the Nb electrode. In addition, a Pt/C tip was grown by electron beam-induced deposition (EBID) in a dual-beam FIB. The purpose of the tip is to enable an AFM operation, which is needed for orientation and topographical viewing of the sample. The overall fabrication procedure and junction characteristics are similar to the ones described in Refs. [17,29].

[1] R. P. Huebener, *Magnetic Flux Structures in Superconductors*, Springer Series in Solid-State Sciences Vol. 6 (Springer-Verlag, Berlin Heidelberg, 1979).

[2] A. Bezryadin, Yu. N. Ovchinnikov, and B. Pannetier, Nucleation of vortices inside open and blind microholes, Phys. Rev. B **53**, 8553 (1996).

[3] I. V. Grigorieva, W. Escoffier, J. Richardson, L. Y. Vinnikov, S. Dubonos, and V. Oboznov, Direct observation of vortex shells and magic numbers in mesoscopic superconducting disks, Phys. Rev. Lett. **96**, 077005 (2006).

[4] I. S. Aranson, A. Gurevich, M. S. Welling, R. J. Wijngaarden, V. K. Vlasko-Vlasov, V. M. Vinokur, and U. Welp, Dendritic flux avalanches and nonlocal electrodynamics in thin superconducting films, Phys. Rev. Lett. **94**, 037002 (2005).

[5] I. S. Veshchunov, W. Magrini, S. V. Mironov, A. G. Godin, J.-B. Trebbia, A. I. Buzdin, Ph. Tamarat, and B. Lounis, Optical manipulation of single flux quanta, Nat. Commun. **7**, 12801 (2016).

[6] A. Tonomura, *The Quantum World Unveiled by Electron Waves* (World Scientific, Singapore, 1998).

[7] H. J. Hug, B. Stiefel, P. J. A. Van Schendel, A. Moser, R. Hofer, S. Martin, H. J. Guntherodt, S. Porthun, L. Abelmann, J. C. Lodder, *et al.*, Quantitative magnetic force microscopy on perpendicularly magnetized samples, J. Appl. Phys. **83**, 5609 (1998).

[8] A. Volodin, K. Temst, C. Van Haesendonck, Y. Bruynseraede, M. I. Montero, and I. K. Schuller, Magnetic-force microscopy of vortices in thin niobium films: Correlation between the vortex distribution and the thickness-dependent film morphology, EPL **58**, 582 (2002).

[9] H. Polshyn, T. Naibert, and R. Budakian, Manipulating multivortex states in superconducting structures, Nano Lett. **19**, 5476 (2019).

[10] V. V. Dremov, S. Y. Grebenchuk, A. G. Shishkin, D. S. Baranov, R. A. Hovhannisyan, O. V. Skryabina, N. Lebedev, I. A. Golovchanskiy, V. I. Chichkov, C. Brun, *et al.*, Local Josephson vortex generation and manipulation with a magnetic force microscope, Nature Commun. **10**, 4009 (2019).

[11] B. Kalisky, J. R. Kirtley, E. A. Nowadnick, R. B. Dinner, E. Zeldov, A. S. Wenderich, H. Hilgenkamp, D. M. Feldmann, and K. A. Moler, Dynamics of single vortices in grain boundaries: I-V characteristics on the femtovolt scale, Appl. Phys. Lett. **94**, 202504 (2009).

[12] M. E. Huber, N. C. Koshnick, H. Bluhm, L. J. Archuleta, T. Azua, P. G. Björnsson, B. W. Gardner, S. T. Halloran, E. A. Lucero, and K. A. Moler, Gradiometric micro-SQUID susceptometer for scanning measurements of mesoscopic samples, Rev. Sci. Instrum. **79**, 053704 (2008).

[13] J. R. Kirtley, L. Paulius, A. J. Rosenberg, J. C. Palmstrom, C. M. Holland, E. M. Spanton, D. Schiessl, C. L. Jermain, J. Gibbons, Y. K. K. Fung, *et al.*, Scanning SQUID susceptometers with sub-micron spatial resolution, Rev. Sci. Instrum. **87**, 093702 (2016).

[14] A. Finkler, Y. Segev, Y. Myasoedov, M. L. Rappaport, L. Neeman, D. Vasyukov, E. Zeldov, M. E. Huber, J. Martin, and A. Yacoby, Self-aligned nanoscale SQUID on a tip, Nano Lett. **10**, 1046 (2010).

[15] D. Halbertal, J. Cuppens, M. B. Shalom, L. Embon, N. Shadmi, Y. Anahory, H. R. Naren, J. Sarkar, A. Uri, Y. Ronen, *et al.*, Nanoscale thermal imaging of dissipation in quantum systems, Nature **539**, 407 (2016).

[16] Y. Anahory, H. R. Naren, E. O. Lachman, S. B. Sinai, A. Uri, L. Embon, E. Yaakobi, Y. Myasoedov, M. E. Huber, R. Klajn, and E. Zeldov, SQUID-on-tip with single-electron spin sensitivity for high-field and ultra-low temperature nanomagnetic imaging, Nanoscale **12**, 3174 (2020).

[17] M. Wyss, K. Bagani, D. Jetter, E. Marchiori, A. Vervelaki, B. Gross, J. Ridderbos, S. Gliga, C. Schönenberger, and M. Poggio, Magnetic, thermal, and topographic imaging with a nanometer-scale SQUID-on-lever scanning probe, Phys. Rev. Appl. **17**, 034002 (2022).

[18] P. Maletinsky, S. Hong, M. S. Grinolds, B. Hausmann, D. M. Lukin, R. L. Walsworth, M. Loncar, and A. Yacoby, A robust scanning diamond sensor for nanoscale imaging with single nitrogen-vacancy centres, Nat. Nanotechnol. **7**, 320 (2012).

[19] L. Rondin, J. Tetienne, T. Hingant, J. Roch, P. Maletinsky, and V. Jacques, Magnetometry with nitrogen-vacancy defects in diamond, Rep. Prog. Phys. **77**, 056503 (2014).

[20] J. Tetienne, A. Lombard, D. A. Simpson, C. Ritchie, J. Lu, P. Mulvaney, and L. C. L. Hollenberg, Scanning nanospin ensemble microscope for nanoscale magnetic and thermal imaging, Nano Lett. **16**, 326 (2016).

[21] M. Barbiero, S. Castelletto, Q. Zhang, Y. Chen, M. Charnley, S Russell, and M. Gu, Nanoscale magnetic imaging enabled by nitrogen vacancy centres in nanodiamonds labelled by iron–oxide nanoparticles, Nanoscale **12**, 8847 (2020).

[22] Q. C. Sun, T. Song, E. Anderson, A. Brunner, J. Förster, T. Shalomayeva, T. Taniguchi, K. Watanabe, J. Gräfe, R. Stöhr, *et al.*, Magnetic domains and domain wall pinning in atomically thin CrBr$_3$ revealed by nanoscale imaging, Nat. Commun. **12**, 1989 (2021).

[23] E. Marchiori, L. Ceccarelli, N. Rossi, L. Lorenzelli, C. L. Degen, and M. Poggio, Nanoscale magnetic field imaging for 2D materials, Nat. Rev. Phys. **4**, 49 (2022).

[24] D. Koelle, R. Kleiner, F. Ludwig, E. Dantsker, and J. Clarke, High-transition-temperature superconducting quantum interference devices, Rev. Mod. Phys. **71**, 631 (1999).

[25] J. Wichtman and J. A. Conchello, Fluorescence microscopy, Nat. Methods **2**, 9109 (2005).

[26] M. Müller, V. Mönkemöller, S. Hennig, W Hübner, and T. Huser, Open-source image reconstruction of super-resolution structured illumination microscopy data in ImageJ, Nat. Commun. **7**, 10980 (2016).

[27] H. Blom and J. Widengren, Stimulated emission depletion microscopy, Chem. Rev. **117**, 7377 (2017).

[28] P. Bazylewski, S. Ezugwu, and G. A. Fanchini, Review of three-dimensional scanning nearfield optical microscopy (3D-SNOM) and its applications in nanoscale light management, Appl. Sci. **7**, 973 (2017).

[29] T. Golod, O. M. Kapran, and V. M. Krasnov, Planar superconductor-ferromagnet-superconductor Josephson junctions as scanning-probe sensors, Phys. Rev. Appl. **11**, 014062 (2019).

[30] V. M. Krasnov, Josephson junctions in a local inhomogeneous magnetic field, Phys. Rev. B **101**, 144507 (2020).

[31] R. A. Hovhannisyan, T. Golod, and V. M. Krasnov, Holographic reconstruction of magnetic field distribution in a Josephson junction from diffraction-like $I_c(H)$ patterns, Phys. Rev. B **105**, 214513 (2022).

[32] D. P. Kelly, B. M. Hennelly, N. Pandey, T. J. Naughton, and W. T. Rhodes, Resolution limits in practical digital holographic systems, Opt. Eng. **48**, 095801 (2009).

[33] T. Latychevskaia and H. W. Fink, Practical algorithms for simulation and reconstruction of digital inline holograms, Appl. Opt. **54**, 2424 (2015).

[34] R. C. Dynes and T. A. Fulton, Supercurrent density distribution in Josephson junctions, Phys. Rev. B **3**, 3015 (1971).

[35] R. W. Gerchberg and W. O. Saxton, A practical algorithm for the determination of the phase from image and diffraction plane pictures, Optik **35**, 237 (1972).

[36] J. R. Fienup, Phase retrieval algorithms: a comparison, Appl. Opt. **21**, 2758 (1982).

[37] R. A. Gonsalves, Small-phase solution to the phase retrieval problem, Opt. Lett. **26**, 684 (2001).

[38] T. Golod, A. Rydh, and V. M. Krasnov, Detection of the phase shift from a single Abrikosov vortex, Phys. Rev. Lett. **104**, 227003 (2010).

[39] T. Golod, A. Pagliero, and V. M. Krasnov, Two mechanisms of Josephson phase shift generation by an Abrikosov vortex, Phys. Rev. B **100**, 174511 (2019).

[40] T. Golod, R. A. Hovhannisyan, O. M. Kapran, V. V. Dremov, V. S. Stolyarov, and V. M. Krasnov, Reconfigurable Josephson phase shifter, Nano Lett. **21**, 5240 (2021).

[41] G. R. Berdiyorov, M. V. Milošević, L. Covaci, and F. M. Peeters, Rectification by an imprinted phase in a Josephson junction, Phys. Rev. Lett. **107**, 177008 (2011).

[42] C. Di Giorgio, A. Scarfato, M. Longobardi, F. Bobba, M. Iavarone, V. Novosad, G. Karapetrov, and A. M. Cucolo, Quantitative magnetic force microscopy using calibration on superconducting flux quanta, Nanotechnology **30**, 314004 (2019).

[43] J. R. Clem, Josephson junctions in thin and narrow rectangular superconducting strips, Phys. Rev. B **81**, 144515 (2010).

[44] A. A. Boris, A. Rydh, T. Golod, H. Motzkau, A. M. Klushin, and V. M. Krasnov, Evidence for nonlocal electrodynamics in planar Josephson junctions, Phys. Rev. Lett. **111**, 117002 (2013).

[45] N. Nakajima, Improvement in evaluating the logarithmic Hilbert transform in phase retrieval, Opt. Lett. **11**, 600 (1986).